

Measurement of Heat Flux in Reacting Flow in a Backward-Facing Step Combustor

Jennifer Colborn* and Jacqueline O'Connor†
Pennsylvania State University, University Park, PA, 16802

Heat flux to the combustor liner in gas turbine engines is increasing as core sizes shrink and flame temperatures increase. In addition to the presence of a flame, gas turbine combustors have a wide range of flow features including recirculation, shear layer separation and impingement, and boundary-layer recovery. These all impact the heat transfer to the wall, making modeling and prediction through these different flow features challenging. The current work seeks to quantify total and radiative heat transfer from a flame to the wall in a backward-facing step combustor over a range of operating conditions. Backward-facing step combustors have been used in combustion studies due to the combustor-relevant flow features in a relatively simple two-dimensional geometry. In this study, a heat flux sensor and a radiometer are mounted in the combustor floor to measure total and radiative heat flux, respectively. The Reynolds number and plate temperature were varied and heat flux measurements were conducted through the different combustor zones: recirculation, shear layer impingement, and recovery. High-speed CH* chemiluminescence images were also collected for evaluation of the flame heat release. Radiative and total heat flux increased downstream of the impingement zone, and the temperature of the bottom plate and limited impact on the measured heat flux. Chemiluminescence data showed little impact of Reynolds number and plate temperature on the time-averaged flame shape and proper orthogonal decomposition highlighted the vortical structures shedding from the combustor step.

I. Nomenclature

BFSC	=	Backward-Facing Step Combustor
LES	=	Large Eddy Simulation
POD	=	Proper Orthogonal Decomposition
Re_h	=	Reynolds number
T_{ad}	=	Adiabatic flame temperature, K
T_{gas}	=	Vitiated gas temperature, K
TLCs	=	thermochromatic liquid crystals
T_{plate}	=	Plate temperature, K
u_∞	=	freestream streamwise velocity
x, y, z	=	streamwise, wall-normal, and spanwise direction coordinates, respectively
x_r	=	impingement location
ϕ	=	equivalence ratio

II. Introduction

DU E to the increasing temperatures and pressures in modern gas turbine combustors, prediction of heat transfer to the combustor liner can be very complex. Often the gas temperature will exceed the melting point of the liner materials, requiring complicated cooling schemes and thermal barrier coatings. Both radiative and convective heating drive heat flux to the wall. Convective heat transfer rates vary along the liner due to the various flow features present throughout the combustor, including recirculation, shear layer impingement on the wall, boundary layer growth, and swirl, make convective heat transfer difficult to predict. Radiative heat flux to the wall arises from both luminous and non-luminous

*Graduate Research Assistant, Mechanical Engineering, AIAA Student Member.

†Professor, Mechanical Engineering, AIAA Associate Fellow.

sources: the soot created in the combustion process will radiate, especially at high pressures, and combustion products, including carbon dioxide and water vapor, also radiate. Products and soot concentrations vary dramatically throughout the combustor, making prediction of the radiation heat transfer to the wall challenging.

Studies of combustor liner heat transfer often only consider convective heat transfer [1–3], even though radiative heat transfer has been shown to have a dramatic impact on heat transfer to the wall [4]. Many of these previous studies focus on cooling strategies. For example, using thermochromatic liquid crystals (TLCs), University of Florence investigated the effects of realistic combustor cooling features including slot injection, nozzle pressure drop, and cooling hole angle on the effusion cooling effectiveness, on the wall temperature distribution and found that many of these features could impact effusion cooling effectiveness [1, 5, 6]. Other work investigating the importance of cooling hole angles by Scrittore and Thole focused on local cooling effectiveness due to the interaction between the dilution jets and effusion cooling holes in a wind tunnel with a heated plate [7, 8]. Continued work by Shrager and Thole found that if the dilution jet flow momentum was too high, the local cooling effectiveness near the dilution holes could be impacted due to flow entrainment [9, 10]. These studies highlight the importance of wall cooling interactions, but are done at or near room temperature, neglecting any radiation effects.

To observe radiative heat transfer effects, temperatures must be near combustion-relevant conditions. Most of the work that has considered radiative heat transfer has been computation. For example, work done by Berger et al. [11] simulated a helicopter engine using large eddy simulation (LES) with a discrete ordinate method radiation solver and a conjugate heat transfer solver to evaluate wall temperature; they found that the inclusion of the radiation solver increased the accuracy of the predicted wall temperature when compared to experimental TLC measurements. Other work done at the University of Connecticut focused on deploying Monte Carlo ray tracing solvers with various reacting flow models [12], Reynolds-averaged Navier-Stokes models [13], and LES paired with a thickened flame models [14] has highlighted the importance of including radiative heat transfer in evaluation of liner heat transfer. However, the inclusion of radiation in these studies comes at high computational cost.

Experimental work measuring radiation from flames has largely focused on unconfined flames. Early work evaluated NO_x formation [15, 16] and combustion product formation [17]; these studies used a radiometer to measure global radiation from the flame. Other work from Purdue University focused on line-of-sight radiation measurement using an infrared spectrometer in both partially-premixed [18, 19] and non-premixed flames [20, 21]. More recent work has used infrared cameras to evaluate radiative behavior of flame ignition in both quiescent and cross-flow environments [22, 23]. Mixing effects, fuel composition, and ignition performance have all been observed in these studies, which are very important for evaluating a flame. However, they do not investigate flame-wall interactions and their impact on heat flux to the wall.

To address both the convective and radiative heat flux to the wall in a relevant gas turbine flame configuration, a backward-facing step combustor (BFSC) is used to measure total and radiative heat transfer. Backward-facing step combustors have been widely used due to the nominally two-dimensional flow and relatively simple geometry [24, 25]. As shown in Figure 1, behind the sudden expansion of the step, the flow separates, a shear layer forms that expands and impinge on the bottom wall, creating three distinct flow regions: a recirculation, an impingement, and a recovery region, all of which have different flow characteristics, resulting in varying heat transfer. The flame stabilizes in the shear layer, impinging on the bottom wall. This work is an extension of our previous work in a backward-facing step test section with a vitiated flow, which showed decreased heat transfer in the recirculation region due to the lower velocity and heat transfer increase in the boundary-layer region [26]. The heat transfer increases in the recovery region, but the highest levels are seen at the impingement location. Other studies with a flame have shown up to two-times heat transfer where the flame impinges on the wall [27].

In this paper, we measure the total and radiative heat flux from a flame stabilized by the backwards facing step at a variety of operating conditions. The goal is to make some of the first measurements of wall heat flux in a confined gas-turbine relevant environment, characterizing the impacts that the various flow features present have on the total and radiative heat flux.

III. Experiment Design

A detailed description of the design has been discussed previously [26, 28], so this section provides a brief overview of the key experimental features. The combustor is 30 cm long, 5.8 cm high, and 19 cm wide, with a step height of 2 cm. The test section was designed to ensure two-dimensional flow through the center of the experiment. Previous characterization using particle image velocimetry confirmed two-dimensional flow in the middle eight centimeters of the flow [28]. The sensors are located within this middle section to ensure no three-dimensional flow effects impact heat

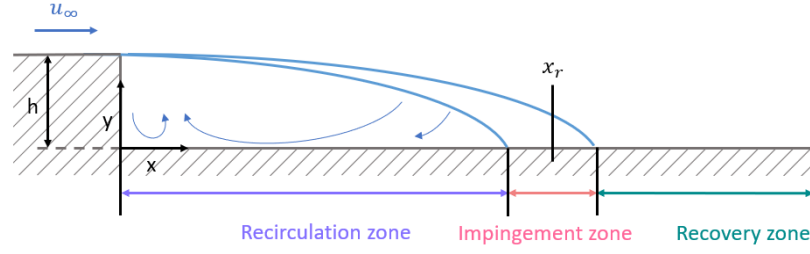


Fig. 1 Schematic of the flow behind a backward facing step - shear layer separation creates recirculation, impingement, and recovery regions.

transfer.

The backward-facing step test section has been used previously to measure total and radiative heat transfer from vitiated gases from a pre-burner. In that configuration, the flow was vitiated so only non-luminous radiation from the hot gases was measured. For this study, the experiment was reconfigured to stabilize the flame in the backward-facing step test section and the flow will no longer be vitiated. Figure 2 shows the new experimental setup: fuel (natural gas) and air are premixed in the pre-conditioning section, then the flow is expanded to enter the test section. An additional hydrogen supply with a high-voltage igniter was used to create a pilot flame for igniting the main combustor. The flame stabilized in the shear layer separating from the trailing edge of the step and impinges on the bottom wall of the combustor. Quartz windows on three sides of the combustor allow for optical access to the flame. To light the experiment, a hydrogen diffusion flame is used as a pilot and igniter. Once the diffusion flame has been stabilized, natural gas is added to the flow until the flame anchors on the step rather than the igniter. At this point, the hydrogen supply and igniter are turned off and the flame will continually run, anchored on the step.

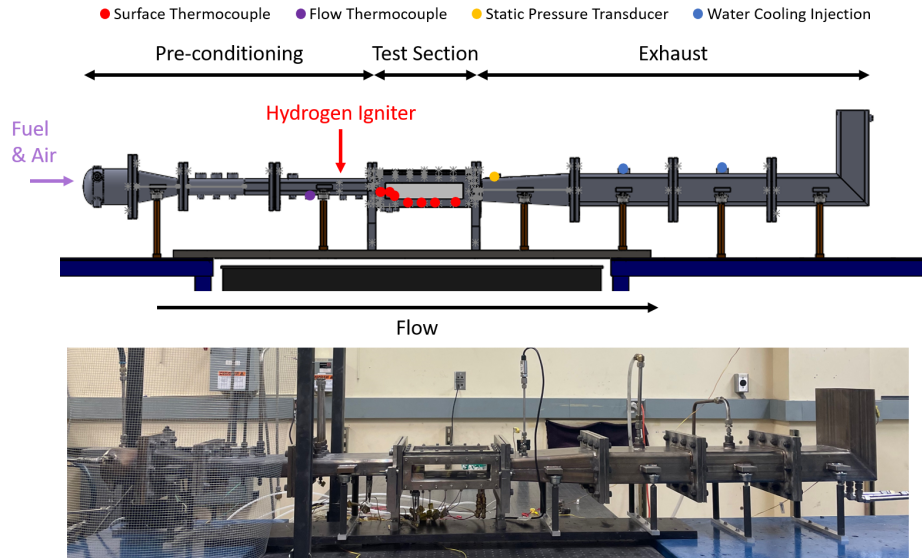


Fig. 2 Schematic of experiment showing flow path and instrumentation.

Also shown in Figure 2 is the instrumentation used: one thermocouple monitors the gas temperature upstream of the test section and thermocouples embedded in the combustor step monitor surface temperatures. Ports in the combustor floor are used to mount the heat flux sensor and the radiometer. Ports are located at four different downstream locations: one in the recirculation zone, one at the shear layer impingement location, and two in the recovery region. Location of the zones was determined using particle image velocimetry [28]. The extra ports that do not have the sensors in place are

filled with plugs, each of which has a thermocouple to monitor the surface temperature. A static pressure transducer is located at the test section exit, and two dynamic pressure transducers are located upstream of the step to monitor for thermoacoustic oscillations.

A radiometer and a heat flux sensor are used to measure radiative and total heat flux, respectively [26]. Manufactured by Vatel, these devices are able to measure incoming heat flux using a circular foil that expands with heat flux, causing a measurable change in voltage. Both sensors are the same, but the radiometer has a sapphire window on top to block out any convective heat transfer to the sensor. The sensors were moved between four ports in the combustor floor to measure heat flux variation through the different flow features: recirculation, impingement, and boundary layer recovery. Location one corresponds to recirculation, two impingement, and three and four are in the downstream boundary layer recovery regime.

Equation 1 was used to calculate the uncertainty of the heat flux measurements. The uncertainty was calculated on a statistical basis using the sensitivity of each measurement to the two parameters varied during testing: plate temperature and Reynolds number. To calculate the sensitivity of the measured heat flux, \dot{Q}'' , to each parameter, a line was fit to the scatter plot of each instance of the measured heat flux data versus the parameter; the slope of the line is the sensitivity. The root-mean-square of the data collected at each operating point was used to capture the variation of each parameter (dT_{plate} and dRe_h). Uncertainty quantification was completed for each sensor at each operating condition and the results are shown in the plots as error bars. If no error bar is visible on a point, it means that the uncertainty is less than the size of the marker.

$$d\dot{Q}'' = \frac{\partial \dot{Q}''}{\partial T_{plate}} dT_{plate} + \frac{\partial \dot{Q}''}{\partial Re_h} dRe_h \quad (1)$$

Finally, the flame is imaged using high-speed CH* chemiluminescence. A high-speed camera (Photron FASTCAM SA1.1) and LaVision high-speed intensifier were used for chemiluminescence. A filter with a center wavelength of 430 nm and filter width of ± 10 nm is used to isolate the signal from CH* chemiluminescence at 5 kHz for one second. Image acquisition was completed using the LaVision software package DaVis 8.

IV. Test Matrix

Initial characterization of the backward-facing step combustor demonstrated relatively narrow stability limits over a range of Reynolds numbers. The adiabatic flame temperature T_{ad} was calculated using Cantera and is conveyed in the colorbar. Figure 3 shows the upper and lower stability bounds of the flame expressed as equivalence ratio, ϕ , versus Reynolds number, Re_h . "Flashback" refers to the upper stability limit. As the fuel flow rate was increased, the flame would begin to move into the separating shear layer and start anchoring on the top of the step. This was also characterized by an increase in combustion oscillation amplitude. The lower limit, referred to as lean blowout (LBO), is characterized by the flame not fully attaching to the step. The flame would not fully blow off, but rather detach on one side before the other. This study was intended to observe heat transfer under steady conditions, so an equivalence ratio of 0.55 was selected for all conditions. Reynolds numbers between 4199 and 8413 were tested, and the surface temperature of the plate, T_{plate} , was varied between 348 and 498K. The longer the combustor was on, the higher the plate temperature. Initial heat flux measurements were taken every 25 K between 348 K and 498 K for heat flux measurements, while chemiluminescence data were taken at 348 K, 423 K, and 498 K.

Table 1 Test matrix for heat transfer experiments.

Condition Number	Re_h	ϕ	T_{ad} [K]	T_{plate} [K]
37	4199	0.54	1559	348-498
38	5249	0.54	1559	
39	6299	0.55	1578	
40	6823	0.55	1578	
41	7350	0.55	1578	
42	8413	0.57	1615	

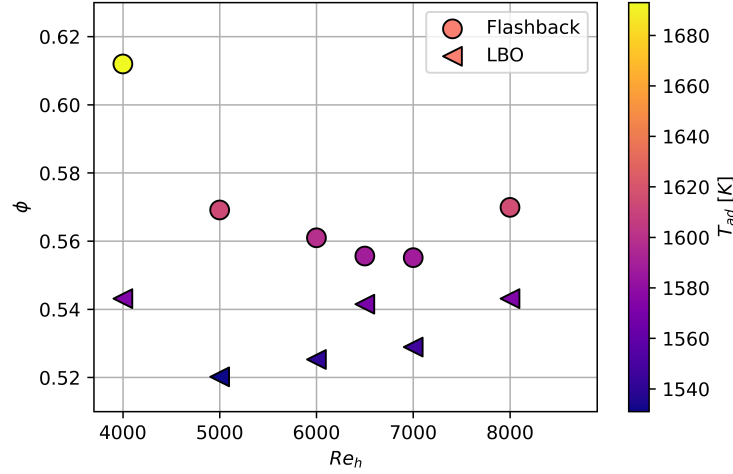


Fig. 3 Upper (flashback) and lower (LBO) stability limits of the combustor as a function of Reynolds number.

V. Results

A. Chemiluminescence Imaging

CH* chemiluminescence data were collected using a Photoron SA1.1 Fastcam with a Lavision High Speed Intensifier, with a 430 nm and filter width of ± 10 nm. Five thousand images were collected at a rate of 5 kHz. Two images were collected to capture the full length of the combustor and are shown for all cases in Figure 4. In the figure, plate temperature increases from left to right and Reynolds number increases from top to bottom. In all cases, the flame stabilizes in the shear layer separating from the step. The flame brush grows rapidly, expanding from its anchoring point until it reaches the combustor floor. After the flame impinges, it lifts off the bottom wall and continues downstream. A noticeable intensity increase is seen for the highest Reynolds number case, $Re_h = 8413$ as compared to the other Reynolds numbers. Otherwise, the flame shape does not change dramatically with either Reynolds number or plate temperature. This result is expected as the range of Reynolds numbers is relatively narrow and the temperature of the plate is not expected to impact the structure of the flame in the main flow.

Proper orthogonal decomposition (POD) was additionally performed on the chemiluminescence imaging data [29]. POD is used to decompose a flow into modes to identify the most energetic behavior of the flow. The two image panes were analyzed separately and plotted together. The sign of the second image was flipped when necessary to ensure the mode shape signs from the first to the second image matched. The first mode, with the highest energy, somewhat mirrors the shape of the chemiluminescence images. These full-flame variations are likely the result of low-frequency “breathing” of the experiment, a result of slow flow rate fluctuations that occur because of the air feed system. In this mode, the flame is seen to anchor off the step, impinge on the bottom wall, and left back off. In the downstream portion some frames do show structures that would suggest vortex shedding is occurring, due to the differences in magnitude of the circular structures.

Modes two and three, however, show strong evidence of vortex shedding. Here, a paired mode of convecting shear layer from the flame oscillations are seen to run into the wall. Together these modes show the vortex shedding off the step, the impingement of the flame on the wall, and the continued vortex structures downstream. This structure is very similar to other the pattern of vortex shedding observed in other backwards-facing step experiments [30–32]. The vortex shedding patterns and wavelengths are similar across all Reynolds numbers. As such, it is expected that all unsteady flame behavior occurs in a similar region for all of the operating conditions considered in this study.

B. Heat Flux Measurements

Heat flux measurements were taken throughout the combustor with varying Reynolds number and plate temperature as described in Table 1. Results from a sample run condition are shown in Figure 6, where plate temperature is 498 K and Reynolds number is 6823. Plotted against downstream location from the step is the total and radiative heat flux. Total heat flux is much higher than radiative in locations downstream of the recirculation zone. Within the recirculation

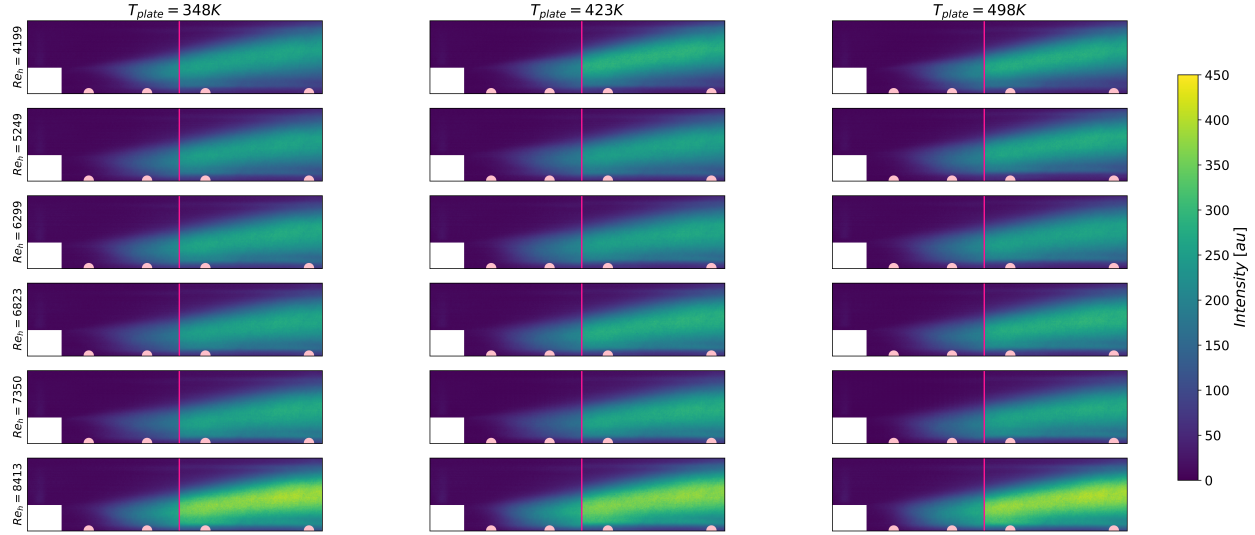


Fig. 4 CH* chemiluminescence imaging of flame. The step in the combustor is shown in white, and the pink line separates the two images collected. Pink circles indicate the locations of the sensors.

region, as indicated by location 1, the measured radiative heat flux is almost zero. This lack of radiative heat flux is likely the result of very few radiating gases present above the sensor. In this location, the flame brush is not very thick and none of the volume of gases directly above the sensor includes significant quantities of reactants, which do not radiate. The highest heat flux is usually seen in location 2, which has been previously associated with the shear layer impingement region in the vitiated heat flux study previously completed [26]. The dramatic increase in total heat flux is likely a result of the flame impingement on the wall, which can be seen from the time-averaged flame images in Figure 4.

Figure 7 shows all measured radiative and total heat flux data plotted as a function of wall temperature. The different locations are indicated with different markers and Reynolds number is conveyed on the color axis. Several trends are visible when observing all the data: first, the radiative heat flux is much lower than the total. The reasons for this result will be discussed in the next section. Second, the recirculation zone, location 1, has much lower heat flux than the other locations. This result is a function of both the lower volume of high-temperature, radiative gases above the sensor as well as the low convective heat transfer that is present in recirculation zones. Third, as the Reynolds number is increased both the total and radiative heat flux increases. This result can be explained by both the effects of higher Reynolds number on convection as well as the fact that the higher Reynolds number flame has a higher thermal power, resulting in more total heat released and hence more heat transferred to the wall.

The trends in heat flux with plate temperature are quite interesting. Neither the radiative nor total heat flux in location one or two is significantly impacted by the plate temperature. The radiative heat flux in location three and four is significantly impacted by the plate temperature, whereas the total heat flux does increase with increasing plate temperature, but proportionally less so than the radiative heat flux. At plate temperatures above 450 K, radiative heat flux in location four becomes greater than locations one and two.

The reason for this change in radiative heat flux can be explained by considering the fields of view of the sensors. Radiometers in locations one and two can observe the hot gases above them, and the upper solid boundary condition is the quartz glass on the top of the experiment. However, the radiometers in locations three and four have the quartz glass as part of their upper boundary condition and the hot metal exhaust section as another part; the sensor in location 4 sees more metal than quartz in its field of view. Downstream of the combustor, the exhaust section of the experiment is made of 316 stainless steel. To raise the plate temperature, the experiment is run for longer times to allow the bottom plate of the experiment, which consists on an inch thick plate of stainless steel, to rise. The temperature of the exhaust section increases as well and will radiate more at these higher temperatures. The heat flux gauges in location four will be exposed to this more than in any other location, which can account for the increase in heat flux seen at higher plate temperatures. Similarly, location three shows some increase in heat flux with plate temperature, but not as much as location four. This result shows that the sources of radiation in the experiment include both the gases and the combustor surfaces.

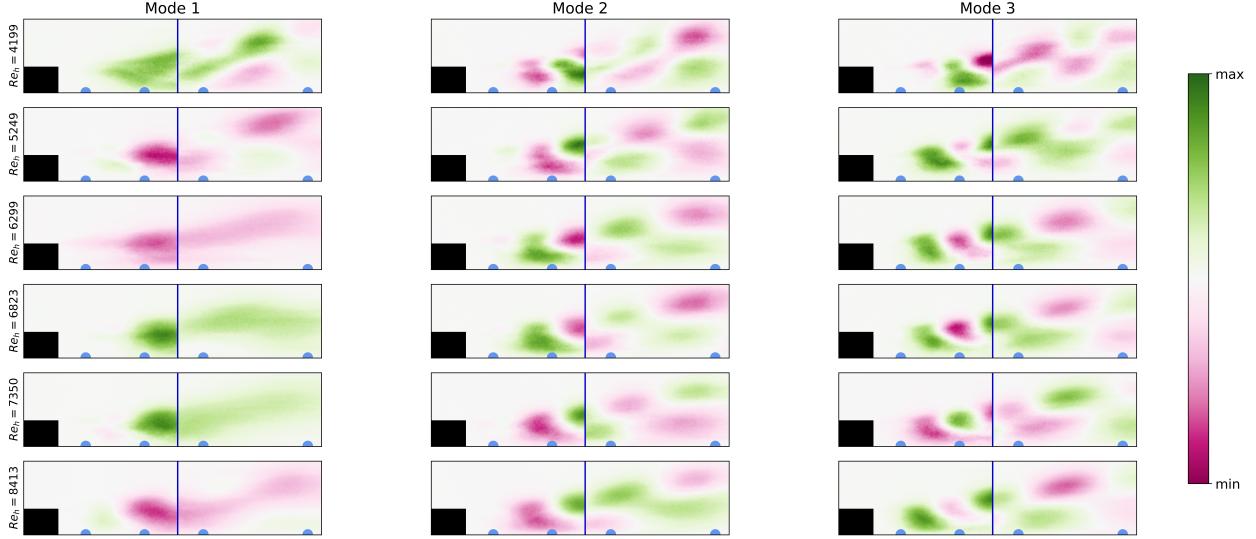


Fig. 5 Proper orthogonal decomposition modes for various Reynolds numbers at $T_{plate} = 498$ K. The black block indicates the combustor step and the blue line separates the two images collected. The blue half circles indicate the locations of the sensors.

In contrast, the total heat flux measurements do not show the same dependence on plate temperature as the radiation measurements. Location two shows the highest heat flux, except at the lowest Reynolds numbers where locations two through four are similar. From an experimental standpoint, it takes longer to raise the plate temperature at a lower Reynolds number, corresponding to more time that the flame was heating the exhaust. The difference in heat flux between location one and the others is dramatic, indicating the effects of the recirculation zone on heat flux to the wall.

C. Impacts of the Flame on Heat Flux

The chemiluminescence imaging shown in Figure 4 aligns with the heat flux data measured through the sensors. The flame anchors on the step and impinges close to location two. When observing the radiative and total heat flux measurements presented in Figure 7, a dramatically smaller heat flux is seen in location one compared to the other locations. The plate does not appear to impact heat flux measurements, rather it is the downstream sections heating up

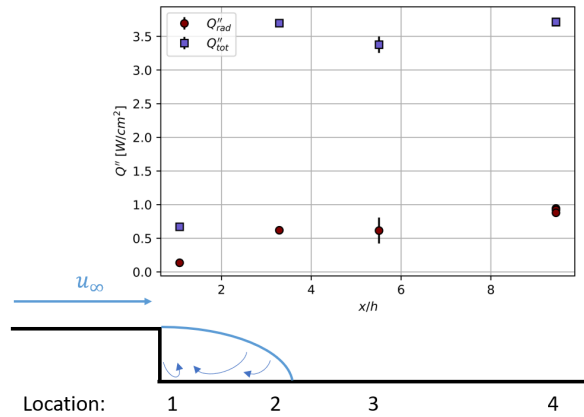


Fig. 6 Radiative and total heat flux versus downstream location for Condition 40 ($Re_h = 6823$) and $T_{plate} = 498$ K. Radiative heat flux is measured with the radiometer, and total heat flux with the heat flux sensor.

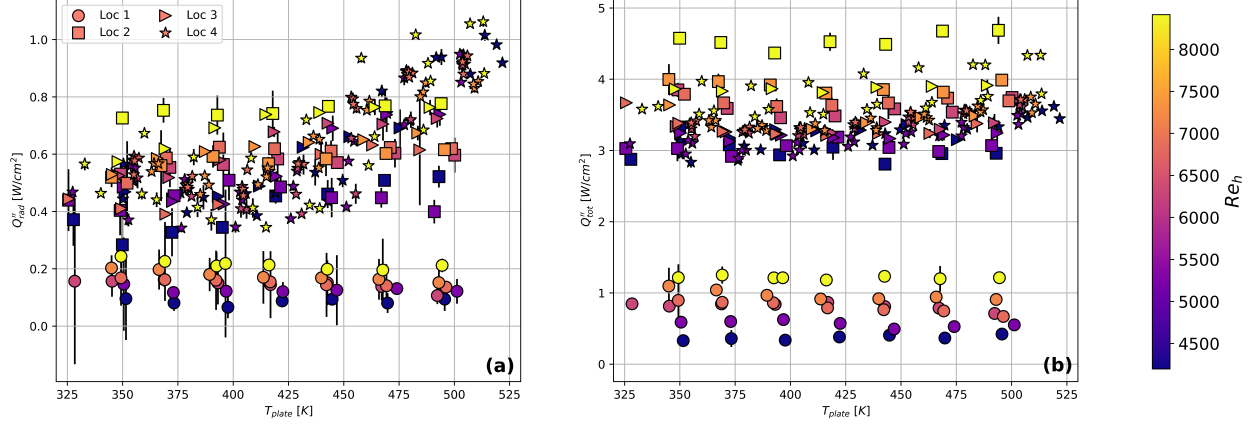


Fig. 7 (a) Radiative heat flux measured by the radiometer versus plate temperature, and (b) total heat flux from the heat flux sensor as a function of temperature. Reynolds number, Re_h is plotted on the color axis.

that are likely causing changes in the heat flux as the wall temperatures rise. Similarly, the chemiluminescence images do not show change with plate temperature.

Previous work completed in this experiment focused on measuring radiative and total heat flux for vitiated flows [26]. In these experiments, the Reynolds number, gas temperature, gas composition, and plate temperature were varied. It was found that the total and radiative heat flux were highly sensitive to gas temperatures, which ranged from 724 K to 1116 K. The composition of the gases was varied through variation in air and CO_2 dilution ahead of the test section, with test cases up to 46% CO_2 in the gases.

When comparing the vitiated cases from the previous study to the measured total and radiative heat flux in the current study, the flame cases have lower maximum values of heat flux. Example ranges of total and radiative heat flux are stated in Table 2 for similar Reynolds number ranges. Several effects could account for this difference. The first major difference between the two experiments is the volume of hot product gases in the combustor. When the experiment is vitiated, the full test section volume is filled with hot product gases. With the flame anchored on the backward facing step, the hot product gases are produced further downstream and in smaller volumes. When looking at Figure 4, the extent of the volume that would have cold gases not contributing to heat flux is greater. This reason also accounts for the reduced heat flux values measured in location one for the vitiated tests. Although the product gases are at higher temperatures in the flame cases, previous simulations have shown that increasing the gas temperature from approximately 1100 K to 1800 K only results in a 30% higher heat flux [33].

Table 2 Ranges of radiative and total heat flux for the vitiated and flame conditions.

Location	Q''_{rad} [W/cm ²]		Q''_{tot} [W/cm ²]	
	Vitiated	Flame	Vitiated	Flame
1	0.3-1.0	0.1-0.2	1.2-3.7	0.3-0.6
2	0.5-1.5	0.3-0.5	2.2-6.5	2.8-3.3
3	0.3-1.3	0.4-0.7	2.1-5.7	3.1-3.4
4	0.3-1.0	0.3-1.0	1.6-4.5	2.8-3.6

Another major difference between the vitiated and the flame tests was the top wall of the combustor. The vitiated tests were performed with a black matte painted stainless steel plate. For the heat flux measurements on the flame, a quartz window had to be placed in the top wall for monitoring of the attachment of the flame. The spectral and material properties of quartz and steel are very different, so a brief study was performed to evaluate the impact of the top surface material. Using the same configuration and some of the test points from the data presented in the previous vitiated studies [26], data was collected using a quartz window on top of the experiment for evaluation of the impact of this boundary condition on the heat flux. Table 3 lists the conditions that were ran with both the steel plate and the quartz window. Heat flux measurements were only collected for location one.

Table 3 Operating conditions for vitiated test cases including variations in Reynolds number, gas and plate temperature.

Condition	Re_h	T_{gas} [K]	T_{plate} [K]
4	3077	853	484
10	3029	1038	481
11	3182	951	479
12	3262	699	478
13	4908	575	479
14	5263	619	480
24	3037	1035	572
25	3193	941	572
26	3182	723	570

Figure 8 shows the comparison of the total and radiative heat flux in location one for the vitiated tests with different upper wall boundary conditions at two different wall temperatures. The heat flux when the experiment was ran with the steel plate is plotted on the y-axis and with the quartz window on the x-axis. The heat flux sensor always reads higher values with the steel plate, except for at the higher plate temperature for the radiometer. While these impacts will be further investigated, the results show the important role that the radiation from the solid surfaces has on the heat flux measurements in the opposing wall.

VI. Conclusions

Heat flux from a natural gas flame was investigated in a backward-facing step combustor. Backward-facing steps capture several of the important flow characteristics including wall impingement, recirculation, and boundary layer recovery that are present in gas turbine combustors, but in a two-dimensional, non-proprietary design that is simpler to model and instrument. The flame anchors on the step in the shear layer formed by the sudden expansion.

Using an approximate equivalence ratio of 0.55 and Reynolds numbers between 4199 and 8413, the impact of both Reynolds number and plate temperature of the experiment were investigated using a heat flux sensor and a radiometer. Both sensors were embedded in the bottom wall of the combustor. Total and radiative heat flux dramatically increased after flame impingement compared to the recirculation region. Both measured heat fluxes increased with Reynolds number and the plate temperature of the experiment has limited effect on the heat flux. For the radiometer in particular, the radiative heat flux does begin to increase as the plate temperature increases in the most downstream location. This is likely due to the increase in temperature of the downstream exhaust, which falls within the radiometers' field of view.

CH* chemiluminescence imaging was additionally used to observe flame dynamics. Corresponding to the heat flux data, the flame impinged on the bottom wall downstream of the previously determined recirculation zone, with very little signal above the recirculation zone, corresponding to the low heat flux measured in that location. Additional analysis using proper orthogonal decomposition highlights the unsteady nature of the flame, as evidenced by the vortical structures shedding off the step in modes two and three.

These results highlight the impact of flow features on heat flux. The dramatically reduced total heat flux in the recirculation zone shows a pocket of low velocity and temperature relative to the downstream locations, and the impacts that radiation outside of the spectral range of the heat flux sensor and convective heat transfer. Further investigation will be completed to determine the flame brush statistics and on the heat flux using OH planar laser-induced fluorescence.

Acknowledgments

This work was funded by the Office of Naval Research under program number N00014-20-1-2278 with program monitor Dr. Steven Martens. We also want to thank Dr. Xinyu Zhao, Nicholas Tricard, and Jonathan Denman from University of Connecticut for helpful discussions.

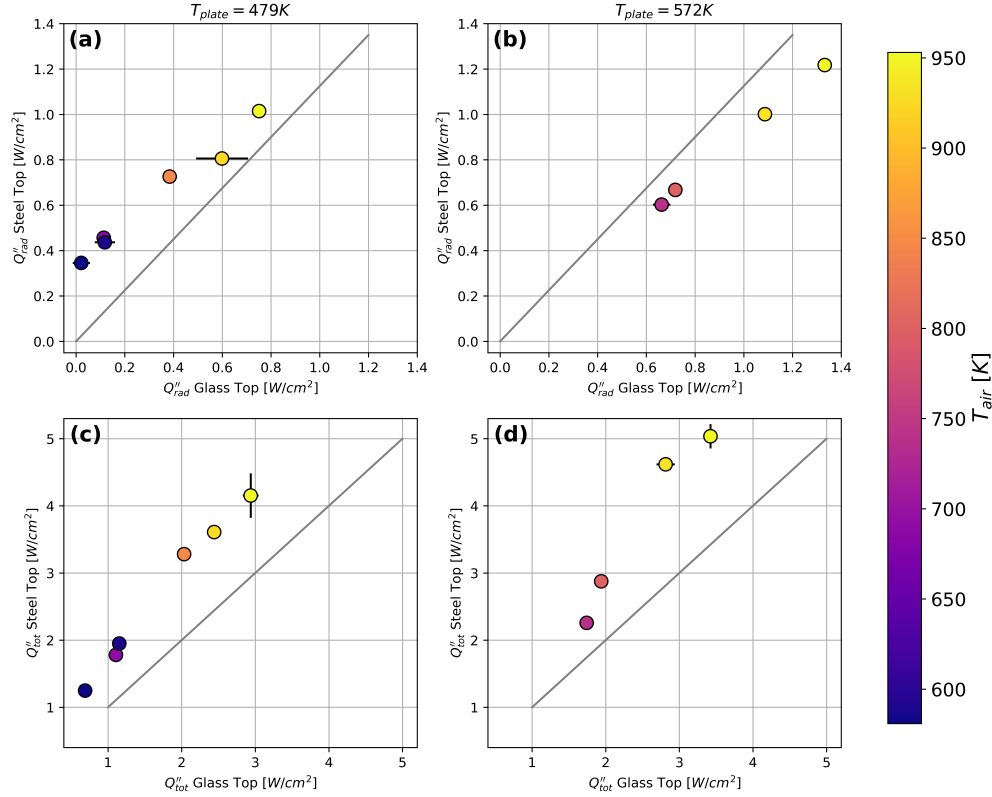


Fig. 8 (a)-(b) Radiative heat flux for the steel plate versus the glass window at $T_{plate} = 479\text{ K}$ and 572 K , (c)-(d) Total heat flux of the steel plate versus glass window at $T_{plate} = 479\text{ K}$ and 572 K .

References

- [1] Andreini, A., Caciolli, G., Facchini, B., Picchi, A., and Turrini, F., "Experimental investigation of the flow field and the heat transfer on a scaled cooled combustor liner With realistic swirling flow generated by a lean-burn injection system," *Journal of Turbomachinery*, Vol. 139, No. 3, 2015, pp. 031012–1–9. <https://doi.org/10.1115/1.4028330>.
- [2] Bailey, J., Intile, J., Fric, T., Tolpadi, A., Nirmalan, N., and Bunker, R., "Experimental and numerical study of heat transfer in a gas turbine combustor liner," *Journal of Engineering for Gas Turbines and Power*, Vol. 125, No. 4, 2003, pp. 994–1002. <https://doi.org/10.1115/1.1615256>.
- [3] Patil, S., Sedalor, T., Tafti, D., Ekkad, S., Kim, Y., Dutta, O., Moon, H.-K., and Srinivasan, R., "Study of flow and convective heat transfer in a simulated scaled up low emission annular combustor," *Journal of Thermal Science and Engineering Applications*, Vol. 3, No. 3, 2011, p. 031010. <https://doi.org/10.1115/1.4004531>.
- [4] Johnson, A. L., and Zhao, X., "Analysis of the Heat Transfer within combustor liners Using a Combined Monte Carlo and two-flux method," *Journal of Turbomachinery*, Vol. 143, No. 3, 2021, p. 031006.
- [5] Andreini, A., Facchini, B., Becchi, R., Picchi, A., and Turrini, F., "Effect of slot injection and effusion array on the liner heat transfer coefficient of a scaled lean-burn combustor with representative swirling flow," *Journal of Engineering for Gas Turbines Power*, Vol. 138, No. 4, 2016, pp. 041501–1–10. <https://doi.org/10.1115/1.4031434>.
- [6] Andreini, A., Becchi, R., Facchini, B., Picchi, A., and Peschiulli, A., "The effect of effusion holes inclination angle on the adiabatic film cooling effectiveness in a three-sector gas turbine combustor rig with a realistic swirling flow," *International Journal of Thermal Sciences*, Vol. 121, 2017, pp. 75–88. <https://doi.org/10.1016/j.ijthermalsci.2017.07.003>.
- [7] Scritture, J., Thole, K., and Burd, S., "Experimental characterization of film-cooling effectiveness near combustor dilution holes," *ASME Turbo Expo 2005*, 2005. <https://doi.org/10.1115/GT2005-68704>.

- [8] Scrittore, J. J., Thole, K. A., and Burd, S. W., "Investigation of velocity profiles for effusion cooling of a combustor liner," *Journal of Turbomachinery*, Vol. 129, No. 3, 2006, pp. 518–526. <https://doi.org/10.1115/1.2720492>, URL <https://doi.org/10.1115/1.2720492>.
- [9] Shrager, A. C., Thole, K., and Mongillo, D., "Effects of effusion cooling pattern near the dilution hole for a double-walled combustor liner - Part I: Overall effectiveness measurements," *Journal of Engineering for Gas Turbines and Power*, Vol. 141, No. 1, 2019, p. 011022. <https://doi.org/10.1115/1.4041148>.
- [10] Shrager, A. C., Thole, K., and Mongillo, D., "Effects of effusion cooling pattern near the dilution hole for a double-walled combustor liner - Part II: Flowfield measurements," *Journal of Engineering for Gas Turbines and Power*, Vol. 141, No. 1, 2019, p. 011023. <https://doi.org/10.1115/1.4041153>.
- [11] Berger, S., Richard, S., Duchaine, F., Staffelbach, G., and Giequel, L., "On the sensitivity of a helicopter combustor wall temperature to convective and radiative thermal loads," *Applied Thermal Engineering*, Vol. 103, 2016, pp. 1450–1459. <https://doi.org/10.1016/j.applthermaleng.2016.04.054>.
- [12] Wu, B., Roy, S. P., and Zhao, X., "Detailed modeling of a small-scale turbulent pool fire," *Combustion and Flame*, Vol. 214, 2020, pp. 224–237. <https://doi.org/10.1016/j.combustflame.2019.12.034>.
- [13] Zhao, X., Haworth, D., Ren, R., and Modest, M., "A transported probability density function/photon Monte Carlo method for high-temperature oxy–natural gas combustion with spectral gas and wall radiation," *Combustion Theory and Modeling*, Vol. 17, 2013, pp. 354–381. <https://doi.org/10.1080/13647830.2013.766365>.
- [14] Wu, B., Roy, S. P., Zhao, X., and Modest, M. F., "Effect of multiphase radiation on coal combustion in a pulverized coal jet flame," *Journal of Quantitative Spectroscopy and Radiative Heat Transfer*, Vol. 197, 2017, pp. 154–165. <https://doi.org/10.1016/j.sqsrt.2017.03.017>.
- [15] Turns, S. R., Myhr, F. H., Bandaru, R. V., and R., M. E., "Oxides of nitrogen emissions from turbulent jet flames: Part II - Fuel dilution and partial premixing effects," *Combustion and Flame*, Vol. 93, No. 3, 1993, pp. 255–269. [https://doi.org/10.1016/0010-2180\(93\)90107-E](https://doi.org/10.1016/0010-2180(93)90107-E).
- [16] Turns, S. R., "Understanding NO_x formation in nonpremixed flames: Experiments and modeling," *Progress in Energy and Combustion Science*, Vol. 21, No. 5, 1995, pp. 361–385. [https://doi.org/10.1016/0360-1285\(94\)00006-9](https://doi.org/10.1016/0360-1285(94)00006-9).
- [17] Edwards, D., and Balakrishnan, A., "Thermal radiation by combustion gases," *Intational Journal of Heat and Mass Transfer*, Vol. 16, No. 1, 1973, pp. 25–40. [https://doi.org/10.1016/0017-9310\(73\)90248-2](https://doi.org/10.1016/0017-9310(73)90248-2).
- [18] Zheng, Y., Barlow, R., and Gore, J. P., "Measurements and calculations of spectral radiation intensities for turbulent non-premixed and partially premixed flames," *Journal of Heat Transfer*, Vol. 125, No. 4, 2003, pp. 678–686. <https://doi.org/10.1115/1.1589502>.
- [19] Rankin, B. A., Magnotti, G., Barlow, R. S., and Gore, J. P., "Radiation intensity imaging measurements of methane and dimethyl ether turbulent nonpremixed and partially premixed jet flames," *Combustion and Flame*, Vol. 161, No. 11, 2014, pp. 2849–2859. <https://doi.org/10.1016/j.combustflame.2014.04.019>.
- [20] Rankin, B. A., Blunk, D. L., and Gore, J. P., "Infrared imaging and spatiotemporal radiation properties of a turbulent nonpremixed jet flame and plume," *Journal of Heat Transfer*, Vol. 135, No. 2, 2013, pp. 021201–1–11. <https://doi.org/10.1115/1.4007609>.
- [21] Zheng, Y., Sivathanu, Y. R., and Gore, J. P., "Measurements and stochastic time and space series simulations of spectral radiation in a turbulent non-premixed flame," *Proceedings of the Combustion Institute*, Vol. 29, No. 2, 2002, pp. 1957–1963. [https://doi.org/10.1016/S1540-7489\(02\)80238-3](https://doi.org/10.1016/S1540-7489(02)80238-3).
- [22] Okhovat, N. S., Hauth, J. M., and Blunck, D. L., "Temperatures of spark kernels discharging in quiescent or crossflow conditions," *Journal of Thermophysics and Heat Transfer*, Vol. 31, No. 1, 2017, pp. 120–129. <https://doi.org/10.2514/1.T4927>.
- [23] Zeuthen, E. D., and Blunck, D. L., "Radiation emissions from turbulent diffusion flames burning vaporized jet and jet-like fuels," *Energy Fuels*, Vol. 31, 2017, pp. 14150–14160. <https://doi.org/10.1021/acs.energyfuels.7b02261>.
- [24] Chen, L., Asai, K., Nonomura, T., Xi, G., and Liu, T., "A review of backward-facing step (BFS) flow mechanisms, heat transfer and control," *Thermal Science and Engineering Progress*, Vol. 6, 2018, pp. 194–216. <https://doi.org/10.1016/j.tsep.2018.04.004>.
- [25] Eaton, J., and Johnston, J., "A review of research on subsonic turbulent flow reattachment," *AIAA Journal*, Vol. 19, No. 9, 1981, pp. 1093–1100. <https://doi.org/10.2514/3.60048>.
- [26] Colborn, J., and O'Connor, J. A., "Variation in convection and radiative heat transfer with Reynolds number and temperature in a backward-facing step combustor," *AIAA SciTech Forum*, 2023. <https://doi.org/10.2514/6.2023-0923>.

- [27] Vogel, J., and Eaton, J., “Combined heat transfer and fluid dynamic measurements downstream of a backward-facing step,” *Journal of Heat Transfer*, Vol. 107, No. 4, 1987, pp. 922–929. <https://doi.org/10.1115/1.3247522>.
- [28] Toumey, J., Zhang, P., Zhao, X., Colborn, J., and O’Connor, J. A., “Assessing the wall effects of backwards-facing step flow in tightly -coupled experiments and simulations,” *AIAA SciTech 2022 Forum*, American Institute of Aeronautics and Astronautics, 2022. <https://doi.org/10.2514/6.2022-0822>.
- [29] Berkooz, G., Holmes, P., and Lumley, J. L., “The proper orthogonal decomposition in the analysis of turbulent flows,” *Annual Review of Fluid Mechanics*, Vol. 25, 1993, pp. 539–575. <https://doi.org/10.1146/annurev.fl.25.010193.002543>.
- [30] McManus, K., and Bowman, C., “Effects of controlling vortex dynamics on the performance of a dump combustor,” *Symposium (International) on Combustion*, Vol. 23, Elsevier, 1991, pp. 1093–1099.
- [31] Altay, H. M., Speth, R. L., Hudgins, D. E., and Ghoniem, A. F., “Flame–vortex interaction driven combustion dynamics in a backward-facing step combustor,” *Combustion and Flame*, Vol. 156, No. 5, 2009, pp. 1111–1125.
- [32] Hong, S., Speth, R. L., Shanbhogue, S. J., and Ghoniem, A. F., “Examining flow-flame interaction and the characteristic stretch rate in vortex-driven combustion dynamics using PIV and numerical simulation,” *Combustion and Flame*, Vol. 160, No. 8, 2013, pp. 1381–1397.
- [33] Colborn, J., O’Connor, J., Tricard, N., Denman, J., and Zhao, X., “Interpreting heat flux measurements in a vitiated backward-facing step flow,” , in review.